The Astrophysical Journal Letters, 871:L28 (6pp), 2019 February 1 https://doi.org/10.3847/2041-8213/aaffcf

Magnetohydrodynamic Simulations for Solar Active Regions using Time-series Data of Surface Plasma Flow and Electric Field Inferred from Helioseismic Magnetic Imager Vector Magnetic Field Measurements

Keiji Hayashi[1,2,3], Xueshang Feng[2,4], Ming Xiong[2,4], and Chaowei Jiang[4]
[1] Key Laboratory of Solar Activity, National Astronomical Observatories, Chinese Academy of Sciences, Beijing 100012, People's Republic of China; keiji@nao.cas.cn, mxiong@swl.ac.cn
[2] SIGMA Weather Group, State Key Laboratory for Space Weather, National Space Science Center, Chinese Academy of Sciences, Beijing 100190, People's Republic of China; fengx@spaceweather.ac.cn
[3] Institute of Space-Earth Environmental Research, Nagoya University, Nagoya, Aichi, 464-8601, Japan
[4] Institute of Space Science and Applied Technology, Harbin Institute of Technology, Shenzhen, 518055, People's Republic of China; chaowei@hit.edu.cn
Received 2018 November 19; revised 2019 January 4; accepted 2019 January 18; published 2019 January 29

Abstract

Temporal evolution of magnetic structures of the solar active region (AR) NOAA AR 11158, is simulated with our magnetohydrodynamic (MHD) simulation models using time-dependent solar-surface electric field or plasma flow data. Using the *Solar Dynamics Observatory*/Helioseismic Magnetic Imager vector magnetogram data, the solar-surface boundary electric field maps are derived with our recently developed algorithm to reproduce the temporal evolution of solar-surface vector magnetic field as observed. The plasma motion velocity maps are calculated through the Differential Affine Velocity Estimator for Vector Magnetograms. In both data-driven models, the simulated evolutionary magnetic field structures at strong-field low-beta regions appear near force-free state, as the current helicity density ($\boldsymbol{J}\cdot\boldsymbol{B}/B^2$) are roughly constant along each field line. Although the magnetic energy simulated with the newly developed plasma-velocity-driven model is about 10% of that by the electric-field driven model, the plasma-velocity-driven model can maintain the frozen-in condition, and evolution of current and free energy generated by the solar-surface plasma motions can be spatially and temporally traced. The present MHD simulation models for AR system can be a step toward better, more realistic data-driven evolutionary modeling, in particular, establishing boundary treatments for introducing the time-dependent observation data in a physically and mathematically consistent manner.

Key words: Sun: activity – Sun: magnetic fields – sunspots

1. Introduction

The magnetic field in a solar active region (AR) system is a primary energy reservoir for coronal eruptive events, such as the solar flare and coronal mass ejections, in which the free magnetic energy is abruptly converted to the kinetic and thermal energy through magnetic reconnection process and/or other instability processes. The magnetic free energy is primarily stored in regions that are characterized with twisted magnetic field structures, and hence electric current density.

The magnetic field in an AR system evolves responding mainly to the two types of solar-surface quantities: the variations of magnetic field and the plasma motions on the solar surface (e.g., Török et al. 2014). The emerging magnetic flux carries the subsurface magnetic energy ($B^2/(8\pi)$) directly to the solar corona. The photospheric plasma motions play crucial roles in the energy build-up processes, specifically in the existing closed-field structures such as filament channels over the polarity inversion line (PIL) and the surrounding arcade magnetic structures of ARs. These two processes are often simultaneously intense in flare-productive ARs.

To quantify the magnetic energy accumulations in ARs, one needs three-dimensional spatial structures and the temporal evolution of an AR system responding to the solar-surface variations. Time-dependent three-dimensional magnetohydrodynamic (MHD) simulations can be a powerful physics-based approach for numerically reproducing the magnetic-field three-dimensional structures in an AR system, which is in general hard to measure directly. By using photospheric observation data to specify time-dependent boundary values, MHD simulation models can reproduce temporal variations of three-dimensional structures of MHD variables in a realistic manner (e.g., Jiang et al. 2016).

One of the tactics for driving the solar-surface magnetic field is to use the electric field ($\boldsymbol{E}$) as $\partial_t\boldsymbol{B}=-\nabla\times\boldsymbol{E}$. An advantage of this tactic is that the divergence-free condition, $\nabla\cdot\boldsymbol{B}=0$, can be preserved easily. Two types of methods can be used to determine the bottom-boundary electric field. The first method is to invert the electric field vectors directly from observed magnetic field variations. We recently developed an algorithm to calculate the electric field vectors whose curl can match fully the temporal variations of the three components of observed solar-surface magnetic field (e.g., Hayashi et al. 2018). With the electric field maps, our MHD simulation model (hereafter called the E-driven model) can simulate the evolution of a three-dimensional AR system with boundary magnetic field matching observations over time. A caveat of the E-driven model is that the simulated MHD variables do not satisfy the frozen-in condition, as the magnetic field on and near the bottom-boundary surface is driven without being coupled with the other (plasma) variables.

The other method is to calculate the solar-surface plasma bulk velocity ($\boldsymbol{V}$) from observed $\partial_t\boldsymbol{B}$ such that the induction equation, $\partial_t\boldsymbol{B}=\nabla\times(\boldsymbol{V}\times\boldsymbol{B})$, will be satisfied. MHD simulations with the solar-surface plasma velocity as the driving parameter can maintain the frozen-in condition and divergence-free condition simultaneously. As the solar-surface plasma motion is one of the major factors in energy build-up

processes in solar ARs (e.g., Leka et al. 1996; Kusano 2002; Demoulin & Berger 2003), the AR simulation driven with $\boldsymbol{V}$ is a powerful physics-based method for studying the energy build-up process.

In this context, we will first attempt to develop a velocity-driven MHD model for AR systems (hereafter called the V-driven model). In our present V-driven model, as a compromise to avoid difficulties in treating the horizontal components of the solar-surface magnetic field, only the vertical component of magnetic field (B_z) on the bottom-boundary surface is driven directly with the given velocity data.

2. Data and Methodology

2.1. Input Data: Helioseismic Magnetic Imager (HMI) Vector Magnetic Field Data and Differential Affine Velocity Estimator for Vector Magnetograms (DAVE4VM)-inferred Plasma Velocity Data

The vector magnetic field data from the HMI on board the *Solar Dynamics Observatory* (*SDO*; Scherrer et al. 2012; Schou et al. 2012) are used as the primary input data in this study. We select a 16 hr period starting from 2011 February 14, 20:00 UT (hereafter referred as $t = +0$) for the presented simulations and analysis. During this period, an X-class flare occurred around February 15, 01:47 UT ($t = +5.78$ hr), near the central meridian viewed from the Earth. The Space weather HMI AR Patch (SHARP; Bobra et al. 2014) data set contains various indexes of the ARs and the magnetic vector maps derived from the HMI observations (see also Hoeksema et al. 2014). The *SDO* HMI and Atmospheric Imaging Assembly (AIA; Lemen et al. 2012) data are publicly available at the HMI/Joint Science Operations Center (JSOC) database (http://jsoc.stanford.edu/ajax/lookdata.html), and the set of 12 minute cadence HMI SHARP data used in this study is identified as `hmi.SHARP_720s_CEA[377][2011.02.14_20:00:00_TAI/972m]`. The DAVE4VM (Schuck 2008) is used to determine solar photospheric plasma motion vectors from the HMI SHARP data set. The SHARP data maps are spatially smoothed to reduce the map size to 186 and 94 (approximately 1440 km per pixel) from the original size, 744 and 377 (360 km per pixel), in the x direction (or heliographic longitude) and the y direction (heliographic latitude), respectively. The bottom-boundary time-dependent electric field and DAVE4VM-inferred velocity maps are calculated for the 80 12 minute intervals from these spatially smoothed data. Figure 1 shows the input HMI vector magnetic field and the DAVE4VM-inferred plasma motions at a selected instant ($t = +5$ hr).

2.2. E-driven and V-driven MHD Models

The MHD simulation model in this study utilizes several widely used numerical strategies, such as the Total Variation Diminishing, Monotonic Upstream Scheme for Conservation Laws (MUSCL) and the Finite Volume Method, for achieving numerical stability (see Hayashi 2005, and references therein). The governing equations are the compressive ideal MHD equations with the gravity of the Sun. The specific heat ratio γ is set constant at 1.001 to mimic the near-isothermal situation in the lower solar corona. The initial plasma temperature and number density at the coronal base height ($z = 0$) are set as $T_0 = 2$ MK and $N_0 = 10^{12}$ cm^{-3}, respectively. A larger number density than the actual corona is chosen as a compromise to suppress Alfvén speed and mitigate difficulties in handling extremely low-beta situations ($\beta = P_g/(B^2/8\pi)$). The concept of the projected normal characteristics method (e.g., Wu & Wang 1987) is applied for the top, bottom, and side sub-Alfvénic boundary surfaces.

In the E-driven simulation model (Hayashi et al. 2018), the bottom-boundary magnetic field vectors are driven with the electric field as $\partial_t \boldsymbol{B} = -\nabla \times \boldsymbol{E}$. The bottom-boundary plasma velocity is assumed to be zero, $\boldsymbol{V} = 0$.

The V-driven model uses different bottom-boundary treatments than the E-driven model does for introducing the plasma velocity (or apparent motion of photospheric magnetic features). In our provisional tests, it was hard to achieve full controls of all three components of the simulated magnetic field vector only with the plasma velocity data. This is in part because we do not have enough information on the gradients of magnetic field and plasma flow on and around the photosphere. It is perhaps possible to compensate for the lack of information, although such methods are not immediately available. In this study, therefore, we abandon controlling all three components of bottom-boundary magnetic field. Instead, only the vertical component of magnetic field, B_z, is controlled mainly with the DAVE4VM-inferred plasma motion, as $\partial_t B_z = \hat{z} \cdot (\nabla \times (\boldsymbol{V} \times \boldsymbol{B}))$. The other two components (B_x and B_y) can evolve through the nonlinear MHD interactions with the variables in the neighboring cells in the vertical and horizontal directions. A simple second-order upwind method is applied to calculate the horizontal gradients of the given DAVE4VM-inferred plasma velocity and simulated magnetic field, while the third-order MUSCL method is used for calculating the other spatial derivatives.

Under this boundary setting for V-driven model where three components of $\boldsymbol{V}$ are specified, we apply the projected normal characteristic method in order to determine the temporal variations of the remaining five MHD variables on the bottom boundary. In practice, the temporal variation of B_z can be separately determined from the others; hence, the remaining temporal variations of B_x, B_y, plasma density ϱ, and pressure P_g are to be determined. Under the concept of characteristics (or compatibility relation), we can give the same number of constraints as the number of outgoing MHD wave modes. As the DAVE4VM-inferred plasma speeds (typically <2 km s^{-1}) are mostly smaller than the speed of the slow mode, the number of MHD wave modes directing from the inside of simulation region to outside is three (four) when the given V_z is upward or positive (downward or negative). Specifying three components of $\boldsymbol{V}$ is equivalent to giving three constraints. Hence, one constraint must be given to complete the equation system when $V_z < 0$, and no further constraints can be given when $V_z > 0$. For $V_z < 0$, the adiabatic relationship, $\partial_t\ (P_g/\varrho^{\gamma}) = 0$, is chosen in the present study. Finally, the temporal variations of four variables, ϱ, P_g, B_x, and B_y, are determined from the characteristic equations with negative eigenvalues, $V_z - V_S$, $V_z - V_A$, and $V_z - V_F$ (where V_S, V_A and V_F are the speeds of slow, Alfvén and fast modes), and V_z if $V_z < 0$.

For calculating the variables at the ghost cells at $z < 0$, we choose a zero-gradient assumption ($\partial_z \boldsymbol{B} = 0$ and $\partial_z \boldsymbol{V} = 0$) so that nonphysical magnetic field will not arise.

3. Simulation Sequences and Results

The V-driven and E-driven simulations start with one of three states: (a) the potential field (PF) magnetic field

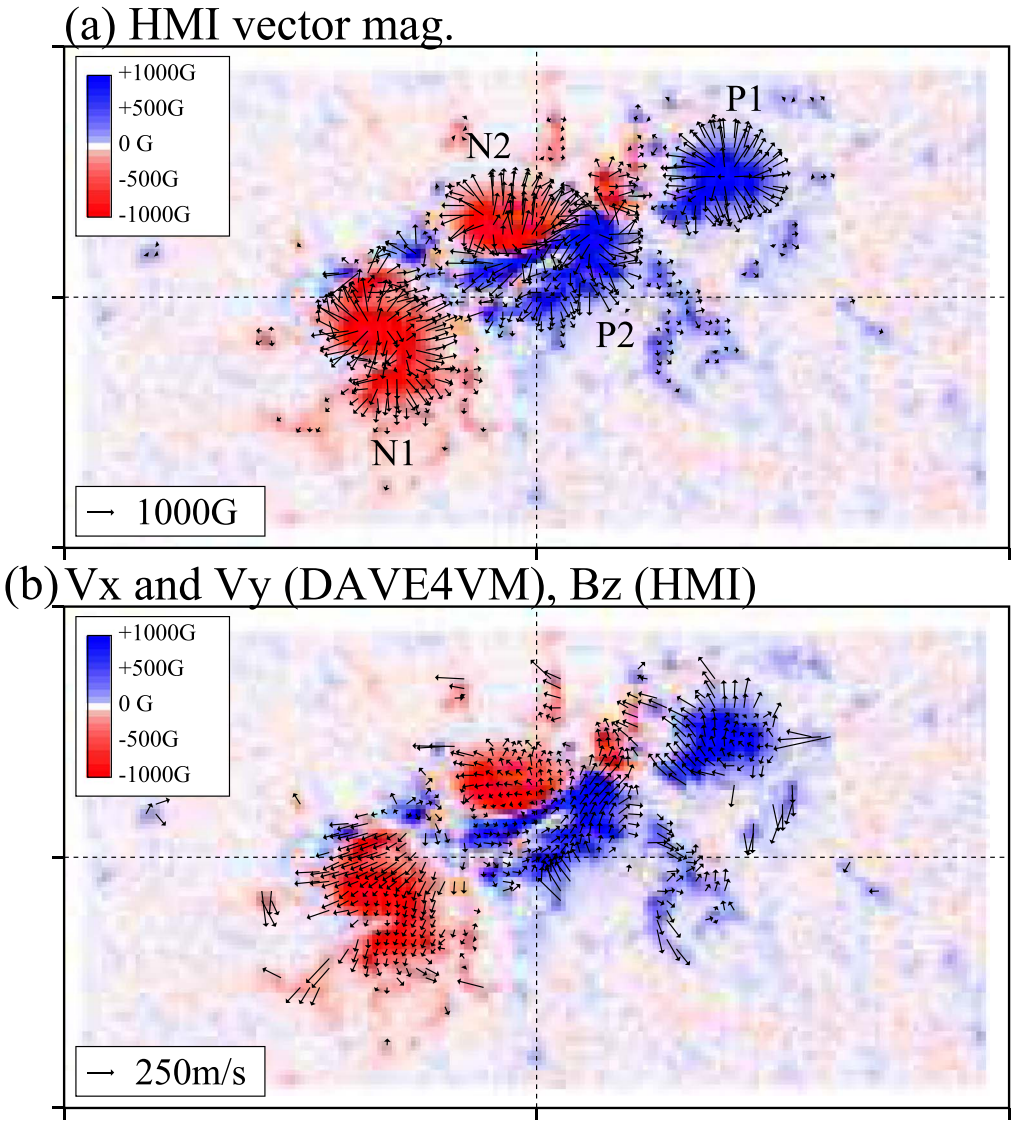

Figure 1. (a) HMI vector magnetic field map at 2011 February 15, 01:00UT (referred as $t = 5$ hr in the text), and (b) the DAVE4VM-inferred plasma velocity from two HMI data maps at 00:48 and 01:00UT. Labels are placed near four major sunspots of positive (P1 and P2) and negative polarity (N1 and N2).

configuration, (b) the relaxed state with E-driven simulation with the fixed bottom-boundary magnetic field after a short E-driven simulation alters B_x and B_y from the PF values to the observed ones (hereafter referred to as the E-relaxed simulation), and (c) the relaxed state with V-driven simulation with zero value of the bottom-boundary plasma velocity (V-relaxed simulation). Figures 2 and 3 show the magnetic field lines of these three initial values (a)–(c), and snapshots of evolutionary V-driven and E-driven simulations. In total we conduct five sequences of simulations: (I) (a) → (b) → (e) the E-driven simulation, (II) (a) → (d) E-driven simulation, (III) (a) → (g) V-driven simulation, (IV) (a) → (b) → (h) V-driven simulation, and (V) (a) → (b) → (c) → (i) V-driven simulation.

3.1. Current Density

Colors on the field lines in Figures 2 and 3 show the current helicity density, $\alpha = (\nabla \times \boldsymbol{B}) \cdot \boldsymbol{B}/B^2$, that shows the relative direction and magnitude of current density with respect to the magnetic field at each position. In these figures, dark blue (brown) color is for positive (negative) α, scaled with logarithm. The largest absolute $|\alpha|$ was about $4\pi/(3 \cdot 10^3\,\mathrm{km})$ and found near the central PIL between the two sunspot regions, P2 and N2 in Figure 1, in the simulation case (e).

The magnitude of α derived with V-driven models is about one order lower than with E-driven models, because of the different treatments for the bottom-boundary B_x and B_y. The E-driven evolutionary simulation sequences, (I) and (II), yield positive α for the field lines connecting the sunspot regions P2 and N2 in the central part of the simulated system. In panels (c), (h), and (i), the V-driven/relaxation simulation sequences, (IV) and (V), succeed this tendency after passing the E-relaxed state.

In panel (g), the sequence (III) V-driven model directly starting from the PF configuration yields a different tendency in the sign of α than the others: positive α is dominant only in the southeastern part of the PIL between P2 and N2, while negative α is dominant in the northern part. Starting from zero α, the sign of α is mainly determined by two factors, local and global rotational motions. When the local horizontal plasma motion at the foot point(s) is counter-clockwise, the magnetic flux gains

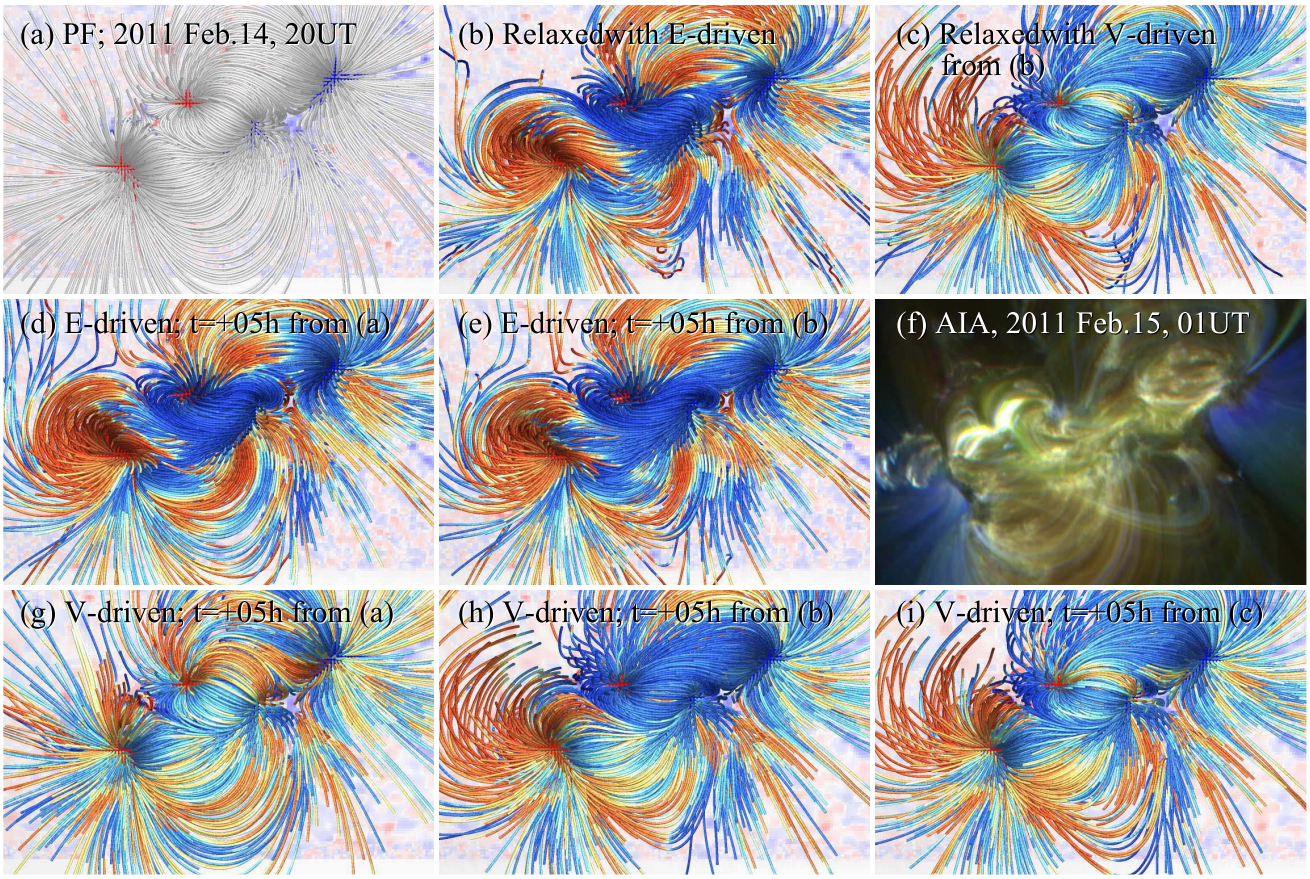

Figure 2. Simulated magnetic field lines, at $z \leqslant 4500$ km, viewed in the approximate Sun–Earth direction. (a) The PF at $t = 0$; (b) the E-relaxed state; (c) the V-relaxation simulation starting from the E-relaxed state (b); (d)–(e) the states at $t = +5$ hr simulated with E-driven model starting from (a) and (b); (g)–(i) the states at $t = +5$ hr with the V-driven model starting from (a)–(c), respectively. The background colors in the simulation are for the bottom-boundary B_z, with blue (red) for positive (negative) B_z, truncated at ± 1000 G. On the field lines, the current helicity density, α ($=\boldsymbol{J}\cdot\boldsymbol{B}/B^2$), is presented with colors in logarithm scale: dark blue (dark brown) for $+(-)4\pi/(10^4$ km), and cyan (yellow) for $+(-)4\pi/(10^5$ km). (f) A three-color composite of AIA 171 Å(blue), 193 Å(green), and 211 Å(red) images at the simulated time $t = +5$ hr as proxy of plasma temperature and density.

the twist of negative α. When the foot point in the south of the PIL moves westward and the other in the north moves in the anti-parallel eastward direction, it is equivalent to giving clockwise local plasma motions at the foot points; hence the magnetic field line will gain the chirality of positive α. Although the magnitude of derived α is much smaller than in the other cases, only the V-driven simulation starting from the PF configuration can display the currents generated purely by the photospheric plasma motions.

In Figure 2, overall the sign of α is constant along each field line, and it seldom changes even when the field lines running parallel in the vicinity have the opposite sign, as two oppositely directed currents repulse each other. This suggests that the simulated magnetic field is, at least in the regions above a certain height from the bottom-boundary surface, overall in the near force-free state, which is attributed to the short Alfvén time. As the Alfvén wave speed at 1000 G and 10^{12} count cm^{-3} is about 1300 km s^{-1}, the simulated MHD variables at the central part of the AR can respond to the given solar-surface variations within 1 minute. In the actual corona and AR, where the plasma number density is much lower, the time required for achieving near force-free state must be shorter. The obtained near-force-free states are similar to those from nonlinear force-free field (NLFFF)-type models (e.g., Sakurai 1981; Wiegelmann et al. 2006; Inoue et al. 2012), though time-dependent MHD models can take into account the presence of plasma and gravity.

In the surrounding arcade magnetic field shown in Figure 3, both a positive and negative sign of α can be found along a single field line. Even in the E-relaxed state (b), an S-shaped field line is cyan (positive α) near the positive sunspot P1 at the upper right and brown (negative α) near the negative sunspot N1. From a test extended E-relaxation simulation, we confirmed that this field line alters the connectivity around $t = 50$ hr, which is much larger than the typical Alfvén timescale. In the evolutionary simulation cases, the field lines with two signs of α are found frequently in the large-scale surrounding magnetic field.

3.2. Magnetic Energy

Figure 4 shows the temporal evolution of the magnetic energy integrated over a volume near the central part of the AR, $\int B^2/(8\pi)dV$. In the left panel, the total energy of (a) the PF magnetic field increases by about 0.35×10^{32} erg as the total absolute of observed solar-surface magnetic field increases. In (b) the E-relaxation simulation, the total energy increases by about 1.5×10^{32} erg. The difference in the energy from the PF configurations corresponds to the free magnetic energy of the evolving magnetic field. The amount of free energy

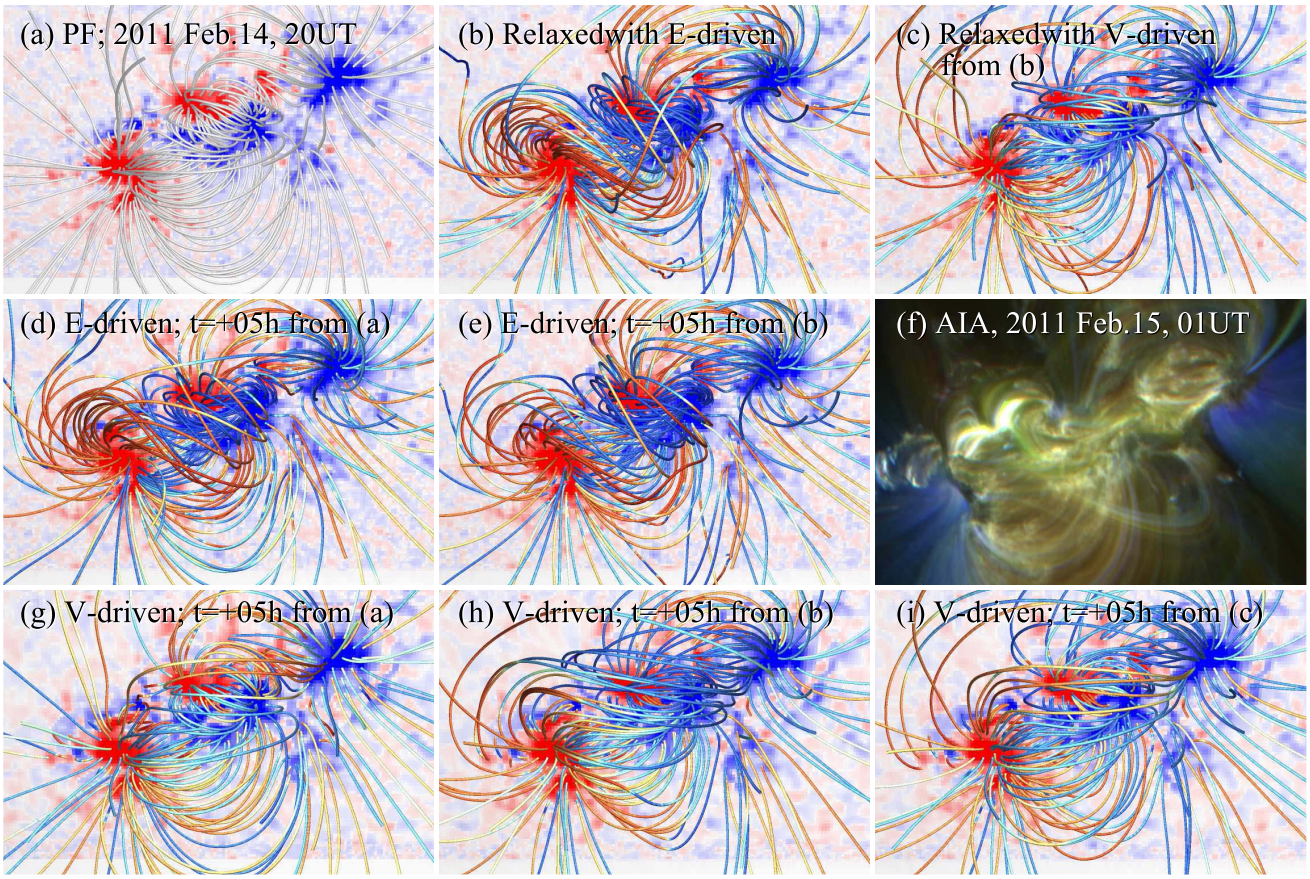

Figure 3. Same as in Figure 2 except that the sparsely selected magnetic field lines at $z \leqslant 16$ Mm are drawn.

obtained with E-driven models (d) and (e) is about $1.5 \sim 2.0 \times 10^{32}$ erg, which overall is consistent with other studies (e.g., Sun et al. 2012).

In the middle panel, we compare the total energy derived from (e) E-driven, (h) V-driven, and (c) V-relaxation simulations, all of which start with (b) the E-relaxed state. Comparing the profiles of the cases (d) and (e), we notice two points. The first point is that the total energy of the case (e) is always larger than the case (d), as the case (e) starts with the state of larger magnetic energy. The second point is that the E-driven model (e) displays two peaks, at around $t = 9$ hr and $t = 13$ hr, while the case (d) shows only the one peak at $t = 13$ hr. The magnetic field configurations derived in the case (e) could more efficiently hold the magnetic energy brought by newly emerging fluxes. For example, more simulated magnetic field fluxes near the bottom boundary direct in the parallel direction to that of emerging ones that are seen as an increase of total absolute (unsigned) flux in Figure 4.

The V-driven/relaxation simulations yield different evolution profiles. The amounts of magnetic energy in the V-relaxation simulation (c) and V-driven simulation (h) quickly decrease. After the constraint imposed on the boundary B_x and B_y is lifted, the twisted magnetic structures start moving upward gradually, and the computational diffusion (or error) reconfigures the magnetic field remaining in the lower simulation volumes to near PF one.

In the right panel, the magnetic energy derived with the V-driven simulation (i) starting from the V-relaxed state (c) is compared with another V-driven simulation starting from the PF configuration (g) and the time series of PF configuration with the simulated B_z of the case (i) (marked with an asterisk in the right panel). The simulation (i) yields higher magnetic energy than the other two. The rather constant difference in energy from the PF configuration indicates that the simulated lower volume overall retains the free energy given at the initial value.

4. Summary and Discussion

We conduct five sequences of evolutionary data-driven simulations and relaxation simulations for the NOAA AR 11158. For this study, we developed a new V-driven model. An advantage of the V-driven model approach is its capability of preserving the frozen-in condition. As many magnetic features, such as the current density distribution, are primarily dependent on the physical conditions at the foot point(s) of the field line, this advantage is important for realistic data-driven/constraint AR modeling. The boundary treatments used in our present study for introducing the observation data as time-dependent boundary values can be a first step toward the better handling of complex solar-surface variations in ARs.

Our present model requires two desired characteristics for better modeling solar ARs. The first one is the inclusion of the realistic thermal heating processes (e.g., Mok et al. 2005), without which plasma temperature and density structures, like those seen in panel (f) of Figures 2 and 3, cannot be reproduced to compare with the actual ones (e.g., Cheung et al. 2015). The plasma structures are critically important for understanding the conversion processes of magnetic energy to the kinetic and thermal ones. The other desired characteristic is the proper handling of the emerging flux, as our present V-driven model can only reproduce flux-cancellations. For this, one needs information on the vertical gradients of MHD

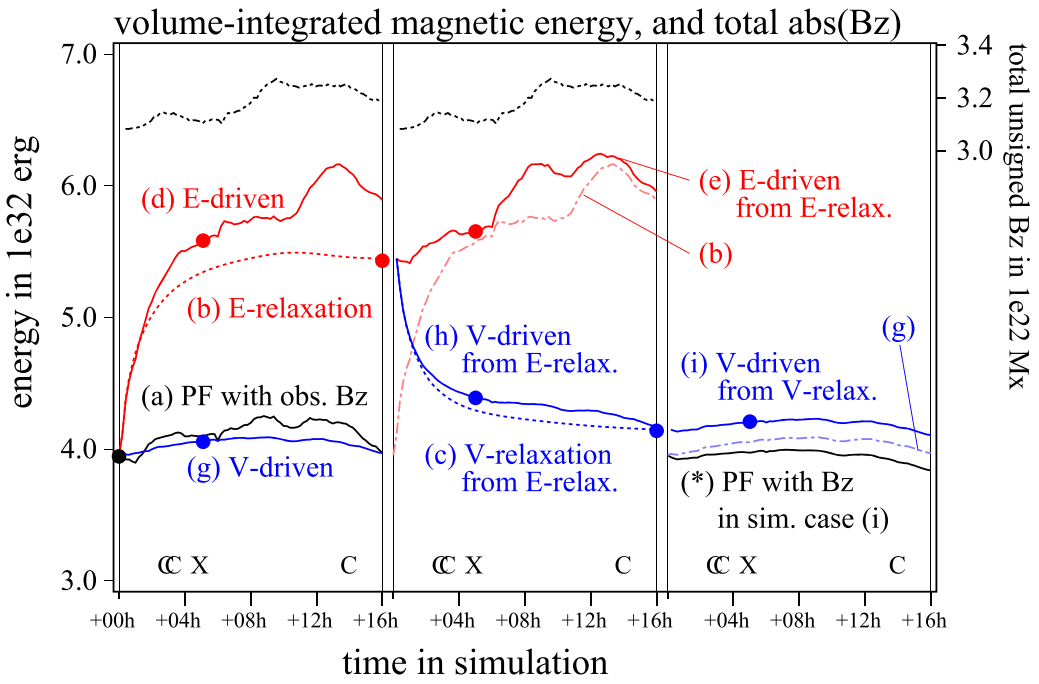

Figure 4. Temporal variations of the magnetic energy, integrated in the volume of 216 Mm × 108 Mm × 46 Mm at the bottom center of the simulation region. The temporal profiles derived with the simulations starting from the PF configuration are shown in the left panel, and those by the simulations starting from the E-relaxed state and V-relaxed state are shown in the middle and right panels, respectively. The labels placed near the profile curves indicate the simulation cases, with a filled circle placed at the instant corresponding to Figures 2 and 3. Solid (dashed) lines are for evolutionary (time-relaxation) simulations, and red (blue) is used for E(V)-driven/relaxation simulations. The dashed–dotted curves in the middle and right panels are duplications of the profile curves of cases (b) and (g). The black solid curves in the left and right panels show the evolution profiles of the PF configurations, with the boundary B_z from the observations (labeled as (a)) and the V-driven evolutionary simulation (i) (marked with an asterisk), respectively. The two identical dashed black curves at the top part of the left and middle panels show the total unsigned B_z of the HMI observation data. The marks (X) and (C) show the approximate times of X and C-class flares in the NOAA AR 11158.

variables around the photosphere. The algorithms that yield the desired information from observations are under investigation (e.g., Kazachenko et al. 2014). New simultaneous multi-wavelength, multi-height observations will directly offer the crucial information. Simulations for the volume crossing the solar surface (e.g., Amari et al. 2004; Abbett 2007; Fan 2009; Toriumi & Yokoyama 2012; Leake et al. 2017) will help determine theory-based vertical gradients. We will improve our MHD model in the future, by incorporating these sophisticated models and new observations in order to enhance our understanding on the energy build-up and conversion processes in AR systems.

We thank the anonymous referee for constructive comments. The HMI and *SDO* data used in this study are courtesy of NASA and the *SDO* science teams. We also thank Dr. Schuck for allowing us to use the DAVE4VM code suite. This work is partially supported by the computational joint research program of Institute for Space-Earth Environment Research, Nagoya University, Japan. The authors are jointly supported by the National Natural Science Foundation of China (grant Nos. 41531073, 41574171, 41731067 and 41874202) and the Specialized Research Fund for State Key Laboratories.

Facilities: *SDO*/HMI, *SDO*/AIA.

ORCID iDs

Keiji Hayashi https://orcid.org/0000-0001-9046-6688
Xueshang Feng https://orcid.org/0000-0001-8605-2159
Ming Xiong https://orcid.org/0000-0001-9427-7366
Chaowei Jiang https://orcid.org/0000-0002-7018-6862

References

Abbett, W. 2007, ApJ, 665, 1469
Amari, T., Luciani, J. F., & Aly, J. J. 2004, ApJL, 615, L165
Bobra, M. G., Sun, X., Hoeksema, J. T., et al. 2014, SoPh, 289, 3549
Cheung, M. C. M., Boerner, P., Schrijver, C. J., et al. 2015, ApJ, 807, 143
Demoulin, P., & Berger, M. A. 2003, SoPh, 215, 203
Fan, Y. 2009, ApJ, 697, 1529
Hayashi, K. 2005, ApJS, 161, 480
Hayashi, K., Feng, X., Ming, X., & Jiang, C. 2018, ApJ, 855, 11
Hoeksema, J. T., Liu, Y., Hayashi, K., et al. 2014, SoPh, 289, 3483
Inoue, S., Shiota, D., Yamamoto, T., et al. 2012, ApJ, 760, 17
Jiang, C., Wu, S. T., Feng, X., & Hu, Q. 2016, NatCo, 7, 11522
Kazachenko, M. D., Fisher, G. H., & Welsch, T. 2014, ApJ, 795, 17
Kusano, K. 2002, ApJ, 571, 532
Leake, J. E., Linton, M. G., & Schuck, P. W. 2017, ApJ, 838, 113
Leka, K. D., Canfield, R. C., & MacClymont, A. N. 1996, ApJ, 462, 547
Lemen, J. R., Title, A. M., Akin, D. J., et al. 2012, SoPh, 275, 17
Mok, Y., Mikic, Z., Lionello, R., & Linker, J. A. 2005, ApJ, 621, 1098
Sakurai, T. 1981, SoPh, 69, 343
Scherrer, P. H., Schou, J., Bush, R. I., et al. 2012, SoPh, 275, 207
Schou, J., Scherrer, P. H., Bush, R. I., et al. 2012, SoPh, 229, 207
Schuck, P. W. 2008, ApJ, 683, 1134
Sun, X., Hoeksema, J. T., Liu, Y., et al. 2012, ApJ, 748, 77
Toriumi, S., & Yokoyama, T 2012, A&A, 539, A22
Török, T., Leake, J. E., Titov, V. S., et al. 2014, ApJL, 782, 10
Wiegelmann, T., Inhester, B., & Sakurai, T. 2006, SoPh, 233, 215
Wu, S. T., & Wang, J. F. 1987, CMAME, 64, 267